EOS Microwave Limb Sounder GHz optics design and field-of-view calibration

Richard E. Cofield, *Member, IEEE,* and Paul C. Stek

***Abstract*— This paper describes the optics design and field-of-view calibration for the GHz module of the Microwave Limb Sounder instrument on NASA's Aura satellite. Details of near field pattern measurements are presented. Estimated systematic scaling uncertainties (3σ) on calibrated limb radiances, due to FOV calibration uncertainties, are below 0.4%. 3σ uncertainties in beamwidth and relative pointing of channels within the GHz module are 0.006° and 0.003°, respectively. The uncertainty in forward model radiances, due to scan dependence of FOV patterns, is less than ± 0.24 K. Refinements to the calibration using in-flight data are discussed.**

***Index Terms*— remote sensing, calibration, near field range, microwave optics.**

I. Introduction

THE Earth Observing System (EOS) Microwave Limb Sounder (MLS) instrument [1], [2] was launched aboard the Aura spacecraft on 15 July 2004. EOS MLS measures thermal microwave emission from the Earth's limb in order to determine composition and temperature of the atmosphere at altitudes between $\sim$8 km and $\sim$90 km.

The GHz module of EOS MLS comprises 5 heterodyne radiometers: 2 centered near 118 GHz (R1A and R1B) plus 3 others at 190(R2), 240 (R3) and 640 GHz (R4), and their shared optical paths out to a 1.6 m$\times$0.8 m diffraction-limited primary aperture. The critical pressure and temperature measurements at 118 GHz are made redundant by observing both polarizations; R1A measures emission polarized vertically (electric field parallel to the nadir vector at the limb tangent point, altitude h_T) and R1B is polarized horizontally. An overview paper [1], describing the EOS MLS experiment, defines the Field of View (FOV) of the MLS instrument as its response to incident radiation as a function of angle. This paper describes the GHz optics design, alignment and performance, and calibration of its FOV on Near Field Range (NFR). A separate module, operated at 2.5 THz, is described in [3]. The co-alignment between GHz and THz FOVs is discussed here.

II. Design

FOV requirements given in [1] fall in two categories: performance requirements on Half Power Beam Width (HPBW), beam efficiency, pointing and FOV scan; and a FOV calibration requirement which limits the allowable errors, induced by imperfect knowledge of the FOV shape, in antenna radiances convolved using representative radiance profiles provided by the science team. Boresight pointing of radiometers in both GHz and THz modules is referred to the $O^{18}O$ line at 234 GHz. In practice, we establish compliance with both sets of requirements from both measurements of the FOV in the ground environment, and analytical models when the space environments (thermal, dynamic, *etc.*) cannot be simulated before launch or for FOV regions that are inaccessible (e.g. far sidelobes) to conventional measurement. For calibration we divide the 4π solid angle domain of the FOV in two parts, conforming to the first two levels of MLS data processing, defined in [1]: The first part is Ω_A, the cone extending $\sim \pm 6^\circ$ about the nominal boresight direction. We provide the antenna directivity $G_b^A(\theta, \phi)$ inside Ω_A to the MLS forward model [4] to produce coefficients used in Level 2 processing to retrieve geophysical parameters. In Ω_A both atmospheric signal and the FOV vary rapidly with angle. Subscript b denotes the band frequency dependence of the FOV functions supplied; an error summary below shows that an even weaker scan angle dependence has little effect in the forward model. For the second part, the region outside Ω_A, we calibrate radiances at Level 1 [5], by integrating far sidelobes over the remaining $4\pi - \Omega_A$. We provide antenna transmissions η_r^{AA} (which have no frequency dependence within each radiometer r, and no scan dependence overall), and ohmic loss terms.

A reflector antenna system was the only candidate considered capable of meeting the FOV calibration requirement with an electrically large aperture ($D \sim 3500\lambda$ at 660 GHz) over a scan range approaching 100$\times$HPBW. The EOS MLS dual offset reflector design avoids blockage, and produces both a compact antenna and a moderately large f/D for multiplexing the radiometer bands quasi-optically. A calibration load sufficiently large to fill the FOV of the GHz antenna would be impractical, so for radiometric gain calibration, the GHz radiometers view warm targets and cold space through optics separate from the primary aperture. Thus, GHz radiometric calibration levies a set of optics-related requirements which do not exist for the THz module, whose calibration and limb views have a common optical path.

A. Antenna

The antenna system for the GHz module has the same offset Cassegrain prescription as did its predecessor, the Upper Atmospheric Research Satellite (UARS) MLS [6], with properties shown in Figure 1. The surface figure and roughness requirements, derived from Ruze scattering theory [7], are tighter than for UARS MLS to accommodate higher frequency

Manuscript received May, 2005; revised November 18, 2002. The research described in this paper was carried out at the Jet Propulsion Laboratory, California Institute of Technology, under a contract with the National Aeronautics and Space Administration.

The authors are with the Jet Propulsion Laboratory, California Institute of Technology, Pasadena, CA 91109-8099. R. Cofield may be contacted at 818-354-5204 or Richard.E.Cofield@jpl.nasa.gov.

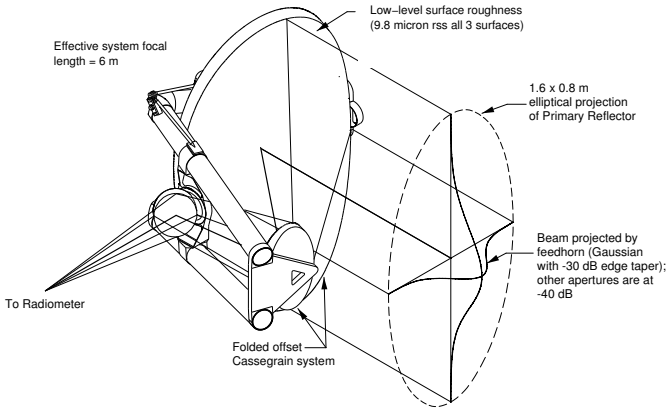

Fig. 1. GHz antenna concept, showing edge tapers and surface tolerances for the EOS MLS reflectors.

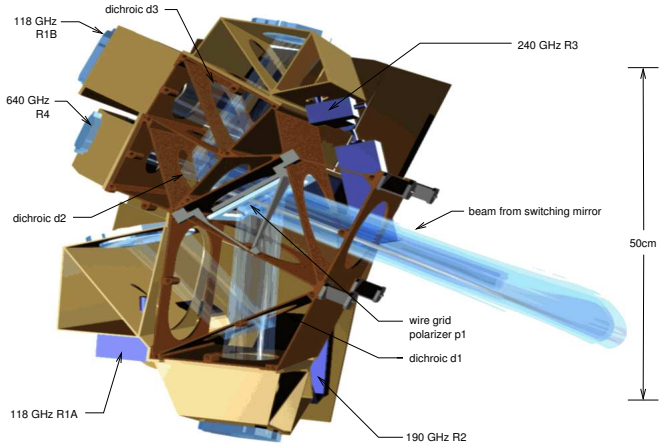

Fig. 2. GHz optical multiplexer and radiometers.

radiometers (240 and 640 GHz), and under-illumination is more extreme for EOS MLS: nominal Gaussian beams are truncated below -30 dB on the primary reflector and -40 dB elsewhere, versus -15 and -20 dB in UARS MLS. The only exceptions are R1A and R1B, where limited space forced the truncation from -30 to -20 dB. On the other hand, the ratio of the required HPBW to λ was larger for R4 than for the lower frequency radiometers. This permitted us to under-illuminate the antenna even further, from -30 to -44 dB. The result was greater margin in beam efficiency, since the 10 μ surface accuracy requirement could have been relaxed at the edge of the aperture. Under-illumination reduces frequency dependent spillovers within the optical system, which complicated the radiometric calibration of UARS MLS [8] and would be worse with the wider bandwidths of EOS MLS.

In Aura's polar orbit, an all-aluminum construction antenna like the one used on UARS MLS would deform in response to orbital variation in solar illumination such that HPBW could vary by 25%. This would cause a global geophysical signature that would be difficult to remove. To minimize thermal distortion, the primary is a lightweight egg-crate structure joining two skins constructed solely of low thermal expansion graphite epoxy. The front surface is bead-blasted for thermal radiative properties, then coated with vacuum-deposited aluminum for high radio frequency (RF) reflectivity, followed by silicon oxide for high IR emissivity. The secondary and tertiary reflectors are solid aluminum with a diamond turned reflective surface and a lightweight truss structure machined on the back. Their front surfaces were then grit-blasted to obtain the desired radiative properties. They are positioned relative to the primary and radiometer chassis on a composite cradle to preserve alignment over temperature and under dynamic loads, while scanning the collimated FOV through Earth's limb.

B. Optical Multiplexer

As for UARS, the incoming signal was split among the GHz radiometers using a multiplexer consisting of a wire grid polarizer and three dichroic plates. Thicknesses, hole patterns, and hole shapes (circular, oval, and rectangular) varied between the dichroic plates to meet bandwidth and insertion loss requirements [9]. The feed mirrors coupling the antenna beam into corrugated horns on the GHz mixers had toric conic prescriptions, like those of UARS, to match the astigmatic beam coming from the 2:1 aspect ratio antenna to the axisymmetric horn patterns. Surfaces at grazing incidence were kept outside the -75 dB contour of the nominal Gaussian beam, and aperture edge tapers at -40 dB (-20 dB for R1B). Figure 2 shows the location of beam splitters, radiometers, and support structure, and indicates the signal beam paths, viewed from the unshaded side of the radiometer chassis with the antenna and covers removed. Figure 6 of [1] shows schematically how the multiplexing is performed.

C. Analytical Model Repertory

We used the optical analysis tools which we had developed for UARS MLS [6], to design the EOS MLS optics and to establish its alignment tolerances. These models included Fraunhofer diffraction and Geometrical Theory of Diffraction (GTD) between Earth's limb and the GHz aperture, Geometrical Optics (GO) between primary and secondary reflectors, and Gaussian Beam Optics (GBO) from the secondary reflector to the feed horn apertures. In addition, we applied models based on Physical Optics (PO), that are now easier to use, more widely available and faster than at the time of UARS MLS development. These tools let us verify component measurements, and substitute analysis for certain measurements that are too difficult or expensive with a large flight instrument.

D. Tolerance methodology

Having verified the design with the GBO propagation module of a commercially available ray-trace program, we formed the overlap integral between two Gaussian beams: one from the nominal feed, and another produced by the forward optics perturbed by misalignments. Evaluating that integral from standard integral tables gives the fractional intensity coupling

between nominal and misaligned beams:

$$\mathcal{I}/\mathcal{I}_0 = \frac{w_{0x}w_{0y}}{w_x w_y} \times \frac{A_{0x}A_{0y}}{|A_x||A_y|}\exp(-C_x - C_y) \times \left|\exp\left(\frac{B_x^2}{A_x}\right)\right| \left|\exp\left(\frac{B_y^2}{A_y}\right)\right| \quad (1)$$

where $A_p = \left[\frac{1}{w_{0p}^2} + \frac{1}{w_p^2}\right] + \frac{j\pi}{\lambda R_p}$
$A_{0p} = 2/w_{0p}^2$
$B_p = j\pi\theta_p/\lambda$
$C_p = (\Delta_p/w_p)^2$
w=Gaussian beam radius at $1/e$ intensity
for $p = x$ and y. Subscript 0 denotes the nominal beam, and the perturbed beam has parameters
θ_p=tilt angles,
Δ_p=decenters, and
θ_p=phase radii.

$\mathcal{I}/\mathcal{I}_0$ is the *Strehl ratio*, from which we supplied an rms wavefront error for the tolerancing algorithm of the program, thereby generating alignment sensitivities for small rigid-body motions of all optical elements. We inverted and adjusted these, based on manufacturing capabilities, to develop fabrication and assembly tolerances for the optical system.

Performance of the optics under orbital heat loads was predicted by using expected temperature fields, from a thermal model, in a structural model that calculated deformations. In turn, these were input to an optics model that calculated FOV performance. We also modeled moisture changes expected between ground and space environments, dynamic loads expected for launch and in flight, and gravitational loads expected in the FOV calibration configuration. We combined these results with the fabrication tolerance budget, to partition tolerances between pre- and post-FOV calibration activities and to specify the number of measurements required for calibration.

III. Performance Verification and FOV Calibration

A. Alignment

Components of the GHz MLS generally do not have surfaces that are specular in the visible region: antenna reflectors have surfaces roughened for thermal radiative properties, and the grid and dichroic elements are periodic surfaces with spacings far greater than a wavelength of visible light. Hence they must be aligned using mechanical features, or displaced optical fiducial surfaces, related by coordinate transformations. Exceptions are the planar switching mirror and the toric feed mirrors, all with diamond-turned surfaces which are inside the chassis, sheltered from the Sun. Since the feed mirrors distort visible light images, and access to alignment surfaces on the mixer feed horns is limited, we added small fiducial surfaces on the sides of feed mirrors for reference in the receiver alignment described below. The tolerance budget identified receiver alignment as the most critical component to overall performance, so it was the only alignment performed using coherent RF sources, rather than mechanical or optical techniques. End-to end alignment was verified in FOV calibration performed on the Near Field Range (NFR), described below. A final alignment of the GHz and THz boresight directions to the Aura master coordinate system was planned as a contingency, using shims in the installation of modules onto the spacecraft. However, during final module tests and spacecraft integration, alignment cube measurements showed that the alignment of boresights to mounting interfaces (and between interfaces) was within design allocations, so no shimming was required.

1) Antenna Alignment: The surface figure of each antenna reflector was evaluated throughout its fabrication by fitting appropriate conic surfaces to coordinate measuring machine (CMM) data. Optical performance of each best-fit surface is described by 1 or 2 conic constants, plus 5 rigid-body misalignments, expressed in a coordinate system fixed in an alignment prism mounted on the back of each reflector. Antenna assembly included theodolite surveys of all these prisms. This verified that reflector shims, pre-computed from the best-fit surfaces, aligned the reflectors correctly, and defined the output (scan) axis of the antenna. Tooling balls, at locations also measured in these systems, permitted us to monitor the alignment through assembly and test on the GHz module using mechanical metering rods rather than optical equipment. The scan axis and scan bearings were aligned to the radiometer chassis at the limb port interface using optical tooling.

2) Switching Mirror Alignment: The switching mirror was aligned to the limb port and to the 640 GHz radiometer's interface plane using reticle mirrors in tooling matched to each interface datum. At this time the switching angles corresponding to limb and space views were established using alignment telescopes at the two port interfaces.

Alignment of the optical multiplexer was based on CMM data around the clear apertures of beam splitters, combined with measurements of the multiplexer structure. This alignment was verified by insertion loss measurements and by NFR patterns, both described below

3) Receiver Alignment: The GHz receiver front ends (RFEs), included feed mirrors and horns, were aligned during final subsystem assembly in an anechoic chamber built to accommodate far field feed pattern measurements. Both amplitude and phase patterns are required to completely describe the illumination of the antenna by its feed; we obtained them using electronics developed for the subsequent Near Field Range test, at several of the same frequencies. These were referred to mechanical and optical features on the receiver using alignment telescopes and theodolites. To set up the range, an alignment telescope was registered to coordinates formed by axes of roll, azimuth and elevation positioners and two translation stages.

Radiation patterns of the feed horn had been measured relative to gage blocks bonded to the mixer body. Before delivery to the range, the feed mirror, horn/mixer assembly and feed mirror structure were assembled with nominal shims. The co-alignment of the the optical bench mounting interface, mirror, gage block and horn body was verified on a CMM, which related all mechanical features. Next, the RFE was installed on positioners and aligned to the telescope, except in axial position. Using a theodolite, we transferred alignment from the telescope to the transmitter (which now obscured the

telescope).

After establishing co- and cross-polarized angles for transmitter and RFE, we measured principal plane patterns at several intermediate frequencies (IFs), obtaining pointing angles, lateral and axial phase centers and beamwidths. To control these 8 quantities we had 6 degrees of freedom available (2 tilts and 1 defocus at each of 2 interfaces: mixer horn to structure and feed mirror to structure). However, we used only the three mirror shims to adjust pointing angles and the mean axial phase center; changes in the other quantities (lateral phase center, beamwaist separation and beamwidth) were acceptably small. A second round of patterns confirmed the desired change in patterns, or led to a revised set of shims; after 4 iterations learning with the first RFE, we needed only 1 or 2 iterations to align subsequent units.

At this point another CMM dataset verified the desired shimming and established a baseline before environmental (thermal and vibration) tests of the RFE. After these tests, we took a third CMM dataset and measured principal plane patterns to verify no change due to vibration.

4) Feed Patterns: After each RFE was aligned, its FOV was characterized by amplitude and phase patterns in both co- and cross-polarization, out to 20° from boresight. Pattern cut spacing of 22.5° ensured that sampling of the 2:1 beam aspect ratio would be adequate for a subsequent spherical wave expansion (SWE) of the feed pattern about a nominal location of the receiver. A complete set of patterns was measured at each of about 7 frequencies chosen in both sidebands (except for the single sideband receivers R1A and R1B) to cover the expected IF dependence of feed patterns, and to provide a baseline for comparison with aperture distributions measured later on the Near Field Range.

The SWE allows accurate reconstruction of the fields at near and intermediate distances from the receiver, such as at

1) planar elements of the optical multiplexer, and
2) the baffles in the switching mirror cavity, which are limiting apertures for the limb, space, and target views of radiometric calibration.

For example, Figure 3 shows principal plane amplitude cuts at one frequency of the R3 radiometer. For this frequency a set of principal plane feedhorn patterns (co-polarized amplitude and phase) had been measured in horn acceptance testing. Given the nominal circular symmetry of the horn, these two cuts sufficed to generate a complete SWE of the fields which would illuminate the feed mirror, and the figure compares the patterns calculated from Physical Optics scattering of these fields by a nominally aligned feed mirror, with the measured receiver patterns. We attribute differences between these patterns to small asymmetries of the corrugated horn, and to the shim adjustment at the feed mirror mounts which aligned the receiver beam to its mechanical interface with the optical multiplexer.

A fifth curve in each panel of Figure 3 shows the cross-polarized amplitude we expect after the beam passes through the wire grid polarizer *p1*. Subsystem testing of the GHz MLS optics did not include pattern measurement for this combination of multiplexer element with a receiver, since UARS MLS had shown the effect on main beam shape was small; instead

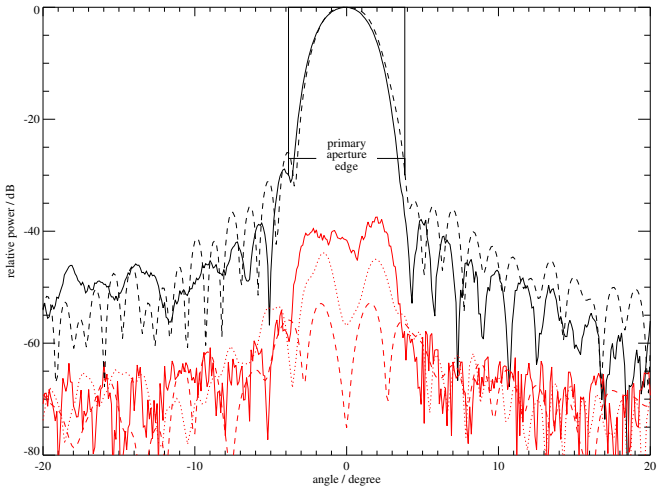

(a) E-plane

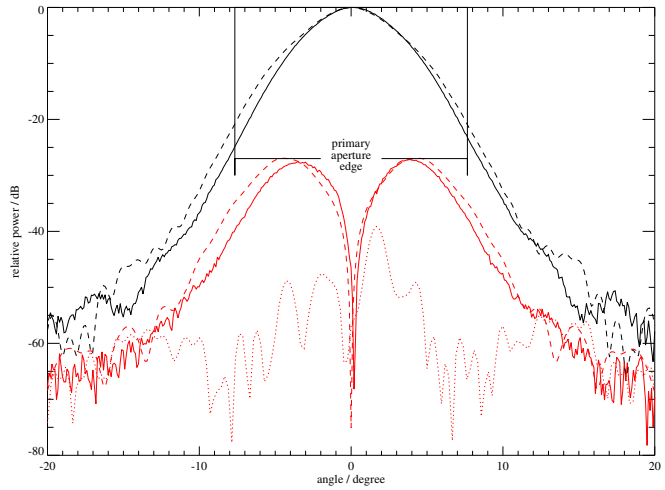

(b) H-plane

Fig. 3. 242.64 GHz feed patterns, co-polarized (black) and cross-polarized (red): measurement during receiver alignment (solid), predicted from measured feed horn pattern using Physical Optics (dashed), and propagated through wire grid polarizer *p1* (dotted, cross-polarized only).

we developed this model after noting surprisingly low cross-polarized power in later near field aperture measurements. The calculation begins with a SWE of the measured RFE patterns. From this we evaluate fields incident on the grid, whose center is located $0.2z_{Rx}$ and $1.7z_{Ry}$ from the principal waists of the nominal feed beam having Rayleigh lengths z_{Rx}, z_{Ry}. Finally we assume ideal behavior of the grid to calculate surface currents and superpose their radiated fields with the incident fields. The resulting far-field patterns are largely unchanged in the co-polarized component, but reduced in cross-polarization, especially on the optical axis, which explains the low values found in near field data. That is, feed pattern cross-polarization, caused by both the curvature and f/D of the offset feed mirror (shown here) and by non-idealities of the dichroic plates, is suppressed by having the

polarizer as the multiplexer element nearest to the switching mirror. The suppression increases for the grid in the far field of the feed beam, hence is least for R1 and greatest for R4. In contrast, UARS MLS had a dichroic in this position and therefore showed peak cross-polarized powers from 10 to 20 dB higher than in EOS MLS.

5) Baffle Transmissions: Feed patterns were integrated to the projected outlines of the antenna reflectors, and of the Limb, Space and Target ports. These provide optical transmissions for radiometric calibration, and for estimating radiance offsets, respectively, in the Level 1 radiance calibration algorithm.

Radiometric calibration uses baffle optical transmissions to calculate power incident on the switching mirror [5]:

$$\dot{P}_i^{MX} = \eta_i^{MX}\dot{P}_i^X + (1-\eta_i^{MX})\dot{P}_i^{BX} \tag{2}$$

where $\eta_i^{MX} = \frac{1}{4\pi}\int_{\Omega_{MX}} G_i^M(\theta,\phi)\,d\Omega$. The feed pattern gain $G_i^M(\theta,\phi)$ in direction θ,ϕ is normalized give 4π when integrated over all solid angle. $\dot{P}_i^X$ is the radiation transmitted through the port (within Ω_{MX}), and $\dot{P}_i^{BX}$ is the radiation in channel i from the baffle in the view X, averaged over the solid angle outside Ω_{MX}. X denotes the switching mirror view: limb ($X = L$), target 1 or 2 ($X = T$), and space ($X = S$). The two target baffles truncate the feed beam with the same outline. Subscript i comprises both channel number and upper or lower sideband, but the frequency dependence if feed patterns is smooth enough that we provide values which are constant over each signal and image sideband.

The limb port radiance $\dot{P}_i^L$ is obtained from a similar equation describing propagation through the GHz antenna. A rigorous form of this equation appears in [5], but to identify FOV-dependent quantities here we simply express the radiance from the antenna, which is incident on the radiometer limb port, in channel i of sideband s (l or u) of radiometer r, as

$$\begin{aligned}\dot{P}_{i,s}^L = {} & \rho_r^1\rho_r^2\rho_r^3\eta_{i,s}^{AA}\eta_{i,s}^1\dot{P}_{i,s}^A \\ & + \rho_r^1\rho_r^2\rho_r^3(1-\eta_{i,s}^{AA})\eta_{i,s}^1\dot{P}_{i,s}^{SA} + (1-\rho_r^1)\rho_r^2\rho_r^3\eta_{i,s}^1\dot{P}_{i,s}^{O1} \\ & + \rho_r^2\rho_r^3(\eta_{i,s}^2-\eta_{i,s}^1)\dot{P}_{i,s}^{S1} + (1-\rho_r^2)\rho_r^3\eta_{i,s}^2\dot{P}_{i,s}^{O2} \\ & + \rho_r^3(\eta_{i,s}^3-\eta_{i,s}^2)\dot{P}_{i,s}^{S2} + (1-\rho_r^3)\eta_{i,s}^3\dot{P}_{i,s}^{O3} \\ & + (1-\eta_{i,s}^3)\dot{P}_{i,s}^{S3}\end{aligned} \tag{3}$$

where
- ρ_r^k = reflectivity of reflector $k = 1,2,3$
- $\eta_{i,s}^{AA}$ = beam efficiency of the antenna system: the product of scattering ($\eta_{i,s}^{AS}$) and diffraction ($\eta_{i,s}^{AD}$) from the primary aperture plane
- $\eta_{i,s}^k$ = spillover efficiency of reflector k with measured feed pattern r
- $\dot{P}_{i,s}^A$ = atmospheric limb radiance
- $\dot{P}_{i,s}^{SA}$ = radiance power from outside FOV measurement angle Ω_A, in the limb hemisphere
- $\dot{P}_{i,s}^{Sk}$ = radiance power illuminating the spillover solid angle for reflector k
- $\dot{P}_{i,s}^{Ok}$ = power thermally emitted by reflector k

TABLE I

ANTENNA AND RADIOMETER BAFFLE TRANSMISSIONS, AND PREDICTED STRAY RADIANCES, FOR EACH MLS RADIOMETER

Reflectivity					
ρ_r^1	0.9977	0.9941	0.9968	0.9926	0.9889
ρ_r^2	0.9977	0.9939	0.9969	0.9924	0.9963
ρ_r^3	0.9984	0.9914	0.9978	0.9893	0.9949
$\prod_{k=1}^3 \rho_r^k$	0.9938	0.9795	0.9914	0.9746	0.9802
scattering and edge diffraction					
η_r^{AS}	0.9997		0.9993	0.9988	0.9916
η_r^{AD}	0.9990	0.9967	0.99986	0.99986	0.99997
η_r^{AA}	0.9987	0.9964	0.9992	0.9987	0.9916
primary spillover					
$\eta_{i,s}^1$	0.9812	0.9787	0.9952	0.9966	0.9972
$\eta_r^{AA}\eta_{i,s}^1$	0.9800	0.9753	0.9945	0.9953	0.9888
η_r^{MX} port baffle transmissions					
$X = L$ Limb	0.99598	0.99344	0.99901	0.99929	0.99907
$X = S$ Space	0.99587	0.99317	0.99903	0.99928	0.99907
$X = T$ Target	0.99575	0.99274	0.99902	0.99929	0.99907

Stray radiances expressed as conventional brightness temperatures (K)

Planck space radiance				
$\dot{P}_\nu^{BB}(2.7°\text{K})$	0.79	0.32	0.16	0.00035
Earth radiance (estimate)				
$\dot{P}_{i,s}^{SA}$	$\dot{P}_\nu^{BB}(150°\text{K})$			
spillover radiance (estimates)				
$\dot{P}_{i,s}^{S1}$	$\dot{P}_\nu^{BB}(100°\text{K})$			
$\dot{P}_{i,s}^{S2}$	$\dot{P}_\nu^{BB}(140°\text{K})$			
$\dot{P}_{i,s}^{S3}$	$\dot{P}_\nu^{BB}(120°\text{K})$			
reflector thermal radiances from flight engineering telemetry				
$\dot{P}_{i,s}^{O1}$	$\dot{P}_\nu^{BB}([-11,+83]°\text{C})$			
$\dot{P}_{i,s}^{O2}$	$\dot{P}_\nu^{BB}([+18,+62]°\text{C})$			
$\dot{P}_{i,s}^{O3}$	$\dot{P}_\nu^{BB}([+10,+41]°\text{C})$			

The ports and tertiary reflector are in the near field of each radiometer front end, by an amount varying inversely with frequency. Therefore, we obtained the integration limit for cut ϕ by propagating the cut-off point (r,ϕ,z) along the nominal Gaussian beam to the far field to get an angle $\theta(\phi)$.

Values of $\eta_{i,s}^k$ and $\eta_{i,s}^{MX}$, for $k = 1,2,3$ and $M = L,T,S$ were interpolated from the measurement frequencies to signal and image sideband centers and provided to flight software. Table I summarizes their average over all bands in each radiometer. The largest change over the full IF range of any radiometer is 0.0015 (for R2). The maximum difference between Limb and Space port transmissions is 0.0003, while the smallest transmission is 0.993; excluding the redundant (and less tapered) R1B, these become 0.0001 and 0.996, respectively.

B. Ohmic Loss

Ohmic loss is a significant factor in radiometric calibration of the EOS MLS GHz module [5]. The loss is greater than for UARS MLS, since the smaller wavelengths of EOS MLS

approach the scale of reflector surface roughness, and since EOS MLS reflector temperatures vary more in the polar orbit.

We inferred ohmic loss of the antenna reflectors from reflectivity measurements in several bands in all GHz radiometers (except R1B), using a radiometric insertion loss technique. The configuration uses the GHz space view in the same way as for for linearity and sideband calibration, described in [5]. The RFE FOVs were switched between an external target, cooled in a liquid nitrogen bath and viewed by reflection at 45° incidence, and an adjacent ambient target. Two witness specimens, delivered with the primary reflector, had undergone the same thermal cycling and bead-blasting as the reflector. No such samples were made with the other reflectors, hence for the pre-launch calculation we substituted the primary's reflectivity, corrected for incidence angle at the secondary and tertiary using the Fresnel plane wave reflection formulæ [10, §4-12].

Reflectivity was found to decrease with frequency, as expected for the loss mechanism being surface micro-structure. Using calculated reflectivities of the silver plate standard, the measured reflectivity ranged from $\rho^1_{R1A} = 0.9983$ to a worst-case value of $\rho^1_{R4} = 0.9839$ with standard deviation of 0.00066.

Discrepancies between the space view and radiances through high-altitude views through the antenna, in two days of special scans soon after Aura launch, led us to revise the pre-launch values for ohmic loss, as discussed below.

C. Radiometric verifications of optics performance

We measured transmission and reflection losses of the multiplexer optical elements on 10–13 December 2001 by exchanging surrogate elements (solid plates and empty apertures) for the splitters while the assembled flight model radiometer viewed hot and cold targets alternately. Measured losses ranged from 0.01 dB (near the measurement threshold) to 0.3 dB, and met all requirements by factors of at least 2.

In two more radiometric tests, performed during integration of the GHz module, we filled the switching mirror and antenna views with loads having sufficient thermal contrast, to confirm that optical transmissions had the high values claimed from feed pattern integration. Detailed results of these tests are discussed in [5].

The first, called the "dual cold load" test, was performed with the antenna removed from the GHz chassis, and nominally identical cooled loads presented to the limb and space ports during a long period of switching between targets and ports. This test confirmed that baffle transmissions were as reported; moreover, using small steps of the switching mirror, it also established how the purity of the space view degrades with mirror angle.

For the second "blue sky" test, both space and antenna views of the complete GHz module were directed near zenith using large folding mirrors outside the door of the assembly facility [5, Figure 10]. For the antenna at each of 3 positions (the center and extrema of its scan range), switched observations were collected over a long period. This test established that the scan dependence of stray light, entering the FOV through spillover and internal reflections within the antenna, was small and had negligible spectral content. This was evident for all radiometers except R4, whose electronics still had problems which prevented it from seeing the full thermal contrast. Since the 640 GHz design edge taper was 15 dB below that at lower frequencies, as confirmed by feed patterns, we were confident that scan dependent spillover was well below the bounds measured for the other radiometers.

D. FOV Calibration Measurements

The field of view was calibrated using a near-field range (NFR) constructed specifically for EOS MLS and assembled within the JPL integration and test (I&T) facility. References [11], [12], and [13] discuss NFR measurement theory, the NFR range built for Aura-MLS by Near-Field Systems (NSI) [14], and the details of the measurement RF techniques respectively. The near-field measurement technique was chosen for the FOV calibration for several reasons. With an antenna measuring 0.8 by 1.6 meters, the far field for the highest frequency in the MLS GHz module (660 GHz) begins at 10 km. Atmospheric attenuation and the geography around JPL preclude measuring the beam patterns in the far field. By locating the NFR in the same clean room as instrument I&T, assembly, spectral calibration, and software checkout were interleaved speeding instrument delivery.

1) Near Field Range Concepts: Briefly, the concept is to feed a tone into the antenna of interest and measure the relative phase and amplitude of the received signal on a defined surface completely enclosing the the antenna. The amplitude in the far field can then be calculated by integrating the contributions from every point. In practical terms, for a high gain antenna with very low edge illumination such as the one used on MLS, virtually all of the radiation focused onto the receivers passes through a plane immediately in front of the antenna. We can then measure the antenna's beam pattern by scanning a source in a plane in front of the antenna. The far field pattern can then by calculated by integrating the complex electric field distribution over the scan plane.

For a high-gain antenna, Kirchoff-Huyghens integration, over the volume bounded by the aperture plane and the far-field sphere, gives a component of the radiated field [11] as

$$F(K_x, K_y) = \iint f(x,y) e^{-i(K_x x + K_y y)}\, dx\, dy \qquad (4)$$

where

F		is proportional to the complex far-zone field component having the same polarization as $f(x,y)$ when $K_x = K_y = 0$
K_x	$=$	$(2\pi/\lambda)\sin\theta\cos\phi$
K_y	$=$	$(2\pi/\lambda)\sin\theta\sin\phi$
$f(x,y)$	$=$	complex aperture field component
θ, ϕ	are	far-field spherical coordinates
x, y	are	aperture position coordinates.

This is exactly a Fourier transform. The integration limits can be reduced from $\pm\infty$ to finite values within which $f(x,y) \neq 0$: typically the aperture size, extended first to include scattering features of the secondary reflector and

support structure, then projected to the scan plan at the 6° angle which bounds Ω_A. In evaluation of (4) using a discrete Fourier transform, the Nyquist theorem gives the spacing of samples required to reduce aliasing within Ω_A. The NSI software also corrects the computed far field for the probe pattern shape; as described in [13], these corrections were small enough that we did not need detailed knowledge of the probe pattern.

2) Near Field Scanner: The mechanical scanner assembly,control electronics, and data acquisition software were procured from Near Field Systems, Inc. (NSI) of Carson California [14].[1] Figure 4 is a drawing of the NSI model 905V-8x8 scanner [12]. The scanner consists of a vertical granite rail that supports a vertical bearing track on which the probe rotation stage traveled. This assembly travels on two horizontal tracks supported by granite beams. The whole assembly is bolted to a $13 \times 13 \times 5$ foot concrete seismic pad that is embedded in the floor, and is mechanical isolated from outside vibration by several inches of absorber. The rails are leveled and straightened through adjustable feet under the rails. The RMS variation of the scanned surface was measured to be less than 5 μm The horizontal, vertical, and angular position of the stage is controlled through an interface box by a 486 PC running DOS that is itself a slave to a Pentium PC that runs the user interface and the NSI data analysis software. A blower delivers room temperature air to cool the motors. Air conditioners maintain the room temperature variations to 1°C or less with temperature cycling on a 20 minute or longer time scale.

3) Electronics Design: We developed phase and amplitude detection systems (interferometers) for each of the four frequencies in the GHz module. In each case the downconverter was the actual flight receiver front end. Directional couplers (10 dB) were permanently added to the coaxial line between the receiver front end and the second IF. The coupled signals were then directed to a breakout panel between the radiator panels. Test points were included in each of the receiver front ends to get the frequency and phase information for the LO.

The frequency and phase information for the source was carried on a 15 foot flexible coaxial cable running from a fixed position on the scanner to the moving probe mount. For each receiver band a temperature controlled test box was built to generate a frequency equal to the difference between the LO and the source. This was then compared to the IF signal from the RFE. The phase and amplitude were measured using an HP 8511 downconverter followed by an HP 8530 microwave receiver.

Figure 5 shows the signal path for the R2 interferometer. The R2 and R3 receivers use the same basic LO design, and multipliers to the submillimeter from the microwave frequencies were available for both receiver bands, so the interferometer design has only minor modifications for the different frequencies, band passes, and multiplication factors.

[1]NSI had previously constructed the NFR for the Submillimeter Wave Astronomy Satellite (SWAS) and the Microwave Instrument for the Rosetta Orbiter (MIRO): a $3x3$ foot portable scanner using a flat granite slab as a reference and operated up to 560 GHz [15]. In addition to a higher frequency, our requirements included a larger 8x8 foot scan area, but without portability.

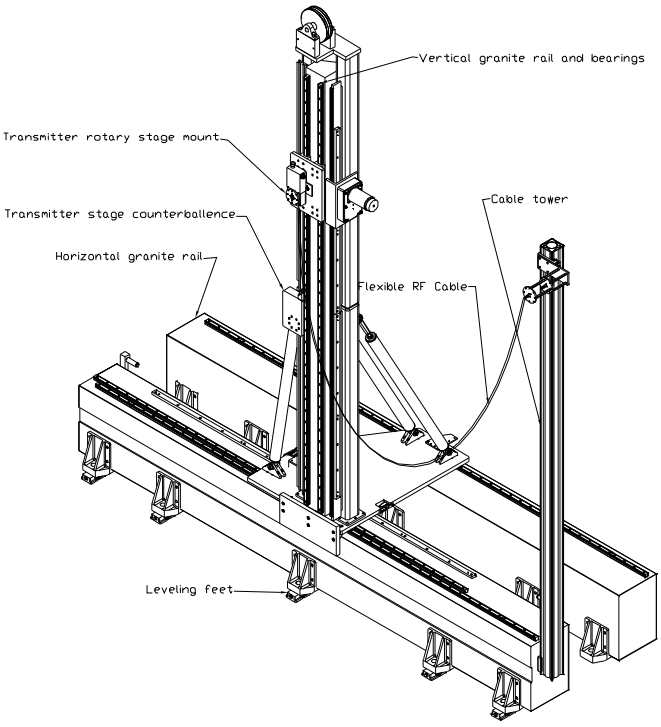

Fig. 4. NSI Model 905V-8x8 Near Field Scanner. The tower scans a total of eight feet horizontally. The probe mount on the tower scans eight feet vertically. Not shown are absorber panels on the tower and in front of the first horizontal granite support. Figure reproduced with permission of NSI.

The R2 and R3 receiver front ends use phase locked Gunn diode oscillators (GDOs) for their LO. The receiver front end downconverter mixers are sub-harmonically pumped meaning that the circuitry in the mixer effectively doubles the LO, so in the case of R2 a 95.95 GHz GDO drives a mixer such that $F_{IF} = |191.9 - F_{RF}|$. A portion of the GDO output is coupled to a detector for monitoring the GDO's output power and to a harmonic mixer that is used to phase lock the GDO to a harmonic of a dielectric resonant oscillator (DRO). The detector can be used as a harmonic mixer. To accommodate this application during FOV calibration, the coaxial line connecting the RFE to the Receiver Control unit (RCO) is looped out and back in the same test port panel used for the IF test signals. A short loop of cable is removed during FOV calibration allowing the detector to be used to sample the GDO signal.

The output from a synthesizer set at a frequency of F_S is fed into a power divider with half of its signal sent to the multiplier on scanner stage where $F_{RF} = 12F_S$ is generated. The IF returned from the R2 RFE has a frequency $F_{IF} = |F_{RF} - 191.9 \text{ GHz}| = |12F_S - 191.9\text{GHz}|$ and carries the phase and amplitude information needed for the measurements. The second output from the power divider is used to pump the detector (being used as a harmonic mixer). The returned IF $F_{\text{Hmix}} = |6F_S - 95.95\text{GHz}| = 0.5F_{IF}$ is separated from the pump signal in a diplexer then doubled to generate the reference signal for the microwave receiver.

4) Scan Plane/Instrument Angle Measurement: While our primary goal was to measure the alignment between the five

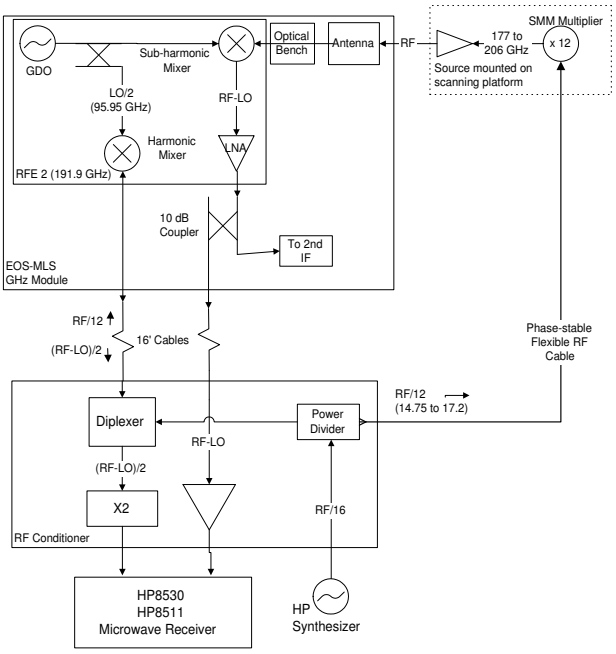

Fig. 5. Simplified block diagram for the interferometer for R2 beam pattern measurements. See text for description of operation.

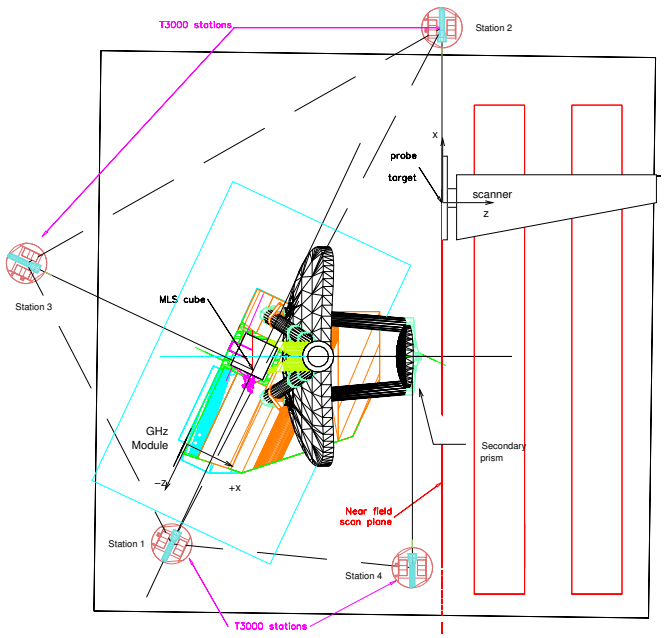

Fig. 6. Plan view of GHz module alignment in near field range.

receivers, we also needed to determine the pointing relative to an alignment cube the spacecraft. This was achieved by comparing a best fit to the plane of the scanner with the location of the alignment cube located near the encoder on the torque tube. Three theodolites were required for this, shown in Figure 6. The master theodolite (station 2) was located roughly in the plane of the scanner approximately 12 feet to the right of the scanner. A target was placed on the support for the probe stage. The probe was then moved to 9 positions on the extremes and center of the scan plane. The elevation and azimuth angles along with their position in the scan plane were recorded for each point. A best fit plane is later determined from these values. Two other theodolites (stations 1 and 3) were positioned to autocollimate with perpendicular faces of the alignment cube and cross collimate with each other and the master station. This established a common azimuth and provided a closure check of the measured angles; at each antenna position, a small translation of the master theodolite in the scan plane made the other stations visible. On a few occasions, a fourth theodolite (station 4) was used to verify antenna alignment, by relating an alignment prism on the back of the secondary to the alignment cube. During calibration periods, theodolite measurements were conducted once in the morning and again in the evening. Generally, any variations were less than the error on our measurements.

5) Testing Procedure: Testing was conducted largely at night to limit the number of people in the test area during scanning, to limit the number of people exposed to noise from the loud scanner motors, and to allow for spectral and sideband calibration along with final assembly efforts during regular work hours. The position was set with a turnbuckle and recorded with the flight encoder. After the antenna was set in position relative to the instrument, the instrument and its support stand were rotated so that the antenna was pointing close to perpendicular to the scan plane. The support structure was then jacked up and lowered onto aluminum blocks placed on the seismic pad. The angle of the scan plane relative to the alignment cube was then measured. Before each set of patterns, a quick pattern at 234 GHz was measured [2] .

During the time to acquire a complete scan (up to 3 hours for R4) the phase drift in the interferometer was sampled periodically by interrupting the scan and returning the probe to a set of 4 positions in the highly illuminated center of the aperture. This technique, called Motion Tracking Interferometry (MTI) in the NSI literature (see [16] for patent information), gives two tilts and one phase offset for each set. These define a best fit plane characterizing both the alignment of the scan plane to the antenna and the total electronics phase shift at that moment. A typical interval between MTI points was 5 minutes. The time series of planar coefficients is used in post-processing to correct the aperture phase distribution to a reference established by the MTI point at the start or end of the scan.

6) Near field pattern results: The 6 or 7 frequencies required to characterize the FOV in each band had generally been duplicated in the RFE pattern characterizations, allowing us to check the models for propagation from feed space to the antenna aperture. Figure 8 compares a measured aperture field to predictions from RFE patterns. Both shape and size of the field amplitude agree within the primary aperture; the cross-polarized distribution is reduced by the polarizing grid

[2]The alignment of the field of view to the instrument is of secondary importance to the alignment of the receivers relative to each other. The 234 GHz line of $O^{18}O$ is MLS's best line for measuring pressure and temperature, so all measurements were referenced to this line.

Fig. 7. GHz Module in the Near Field Range for definitive FOV calibration after environmental tests. The camera was near theodolite station 2 in Figure 6.

as noted previously in Figure 3, with a maximum discrepancy of 5 dB at -40 dB due to model uncertainty in the alignment of grid and feed relative to the antenna.

Cross-polarized patterns were measured at scan angle and frequency spacings coarser than for the co-polarized patterns. Although transmitter roll angles for co- and cross-polarized patterns were orthogonal to within the positioner accuracy of 0.1°, we were unable to measure the probe polarization with respect to scanner coordinates to better than 0.7°. Therefore, polarization angles reported to the flight software have the design values with ±0.5° tolerance due to fabrication.

Figure 9 shows typical near and far-field patterns obtained from the Near Field Range in 118 and 640 GHz bands. Cross-polarized patterns shown in the limb vertical cuts are from adjacent scans matched to the corresponding co-polarized patterns by assuming the transmitter power was unchanged when the probe was rotated 90°; from experience with RFE patterns this is valid for amplitude but not phase. Shadows of alignment tooling balls, on the peripheries of each reflector's clear aperture, can be discerned on the $x = 0$ plane of the amplitude and phase maps at the higher frequency. Background noise in the phase maps shows the aperture plane coverage, expanded to include internal antenna spillover through the secondary support arms, and to capture all appreciable power (from spillover and edge diffraction) which radiates into the ±6° cone about the main far-field beam.

We independently verified the NSI near- to far- field transformation software by introducing measured near field patterns into the optics design software. This allowed us to apply the predicted effects of deformations due to gravity release and orbital thermal loads to the measured patterns. Since these effects were small, and confined to pointing changes, they have not been applied to the patterns for flight software use, but instead are bookkept separately for possible future enhancements of Level 1.

A persistent feature of the R3 far-field patterns was a region of grating lobes within 1° of boresight and 40 dB or more below the main lobe; Figure 10 shows an example. We believe these result from a superposition of images of dichroics *d2* and *d3*, which both lie in the near field of the astigmatic beamwaist produced by the secondary reflector and matched by the feed

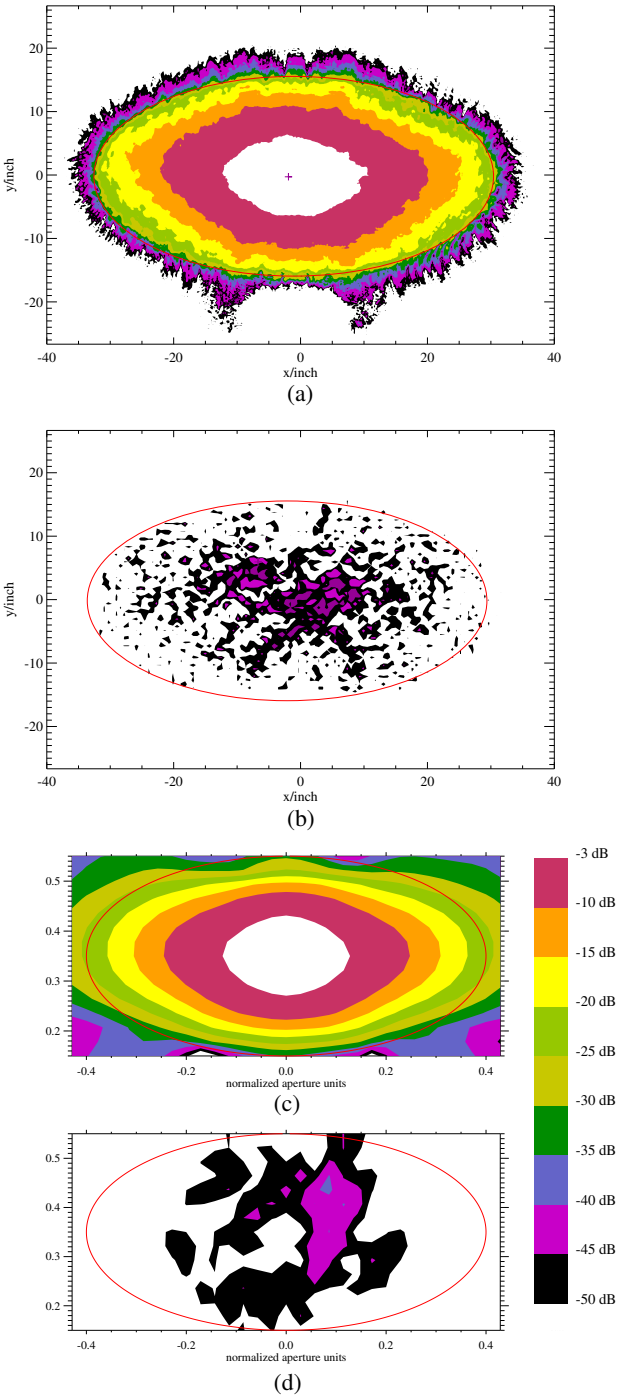

Fig. 8. 242.64 GHz Aperture Field: (a) Co-polarized and (b) cross-polarized amplitudes of the near field measurement compared to (c) co-polarized and (d) cross-polarized projections from RFE patterns. The red ellipses mark the 1.6 m×0.8 m aperture.

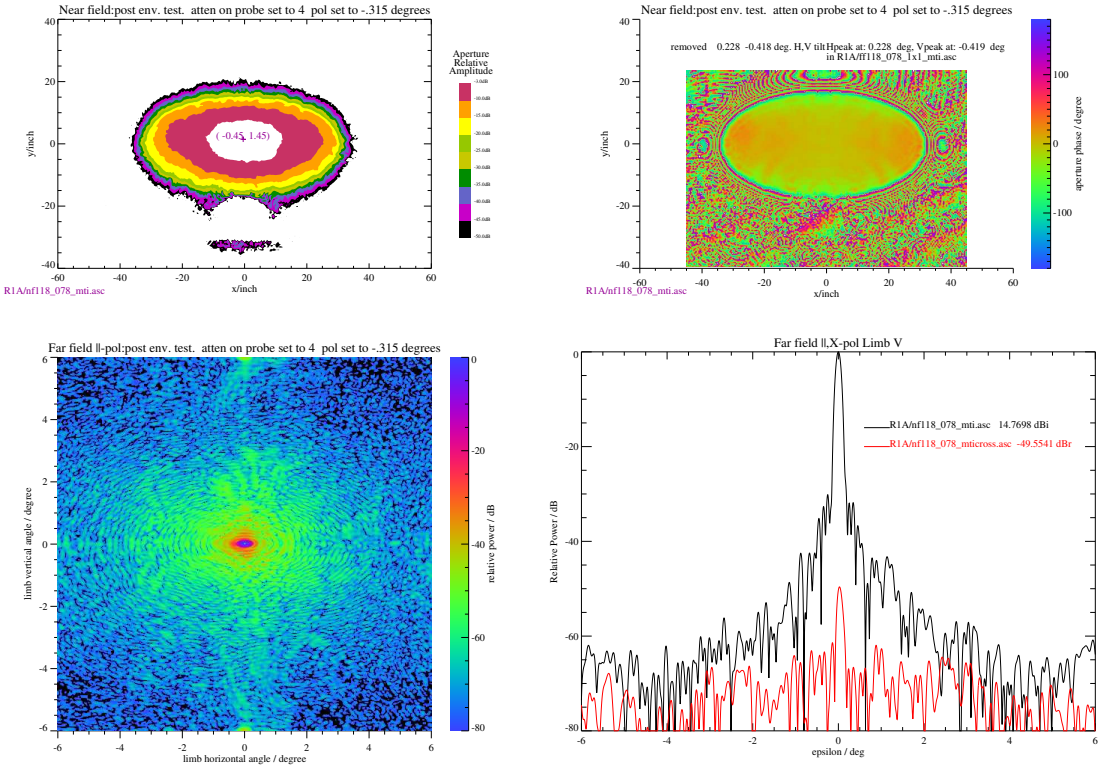

(a) R1A

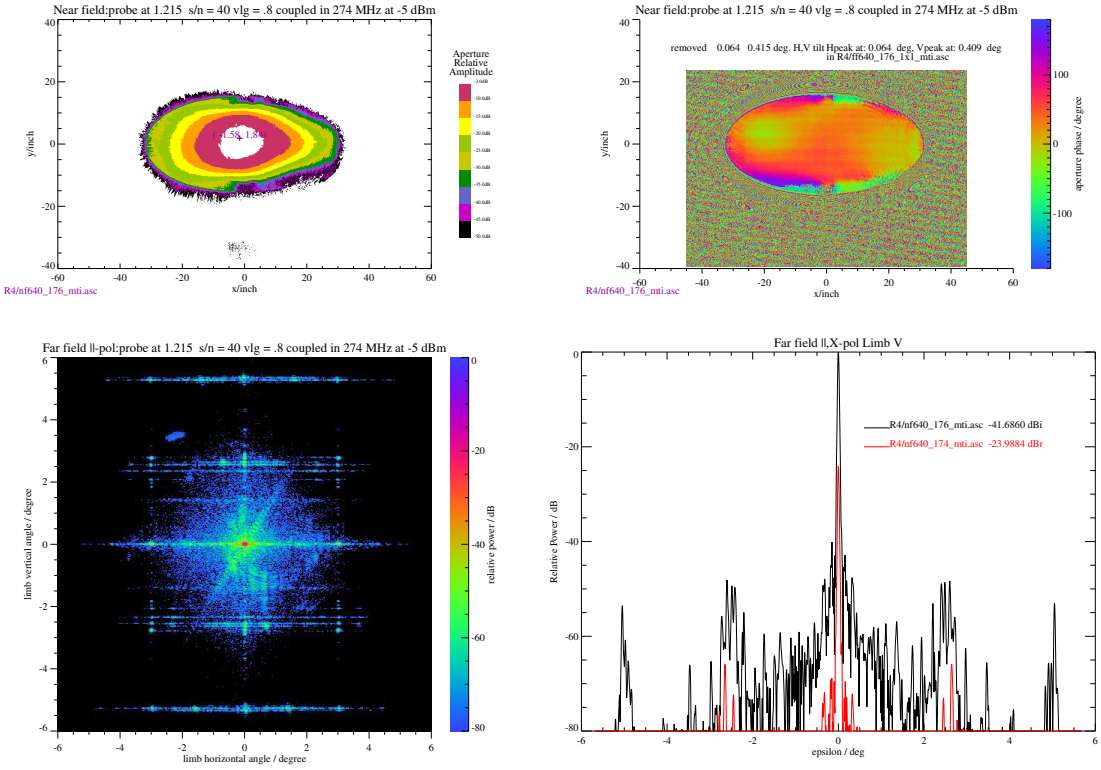

(b) R4

Fig. 9. Near and far field antenna pattern examples at 0 km nominal tangent height for (a) R1A and (b) R4 radiometers. The four panels shown for each radiometer are (clockwise from upper left): near field amplitude, near field phase, far field vertical cut (both polarizations), and far field amplitude map. Faint ripples seen outside the primary aperture ellipse in the near field phase (upper right panels of a and b) result from removing tilts within the aperture, removed for this figure. Since the corresponding amplitudes (upper left panels) are very small, these have no effect on the far field patterns.

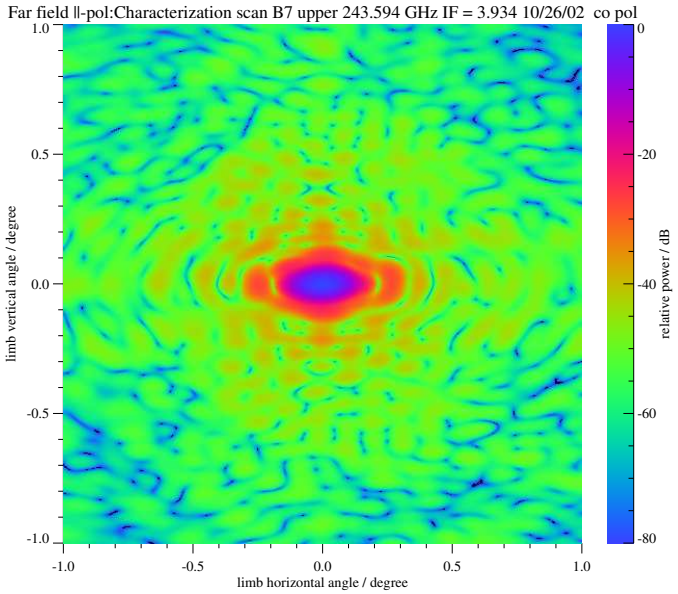

Fig. 10. Main lobe and nearby sidelobes of 240GHz far-field pattern.

mirror. We are currently studying the effect of these lobes on calculated forward model radiances, by applying spatial filters at the beamwaist and aperture.

R4 patterns had other unusual features seen in the far field panels of Figure 9: the diagonal strip through beam center and inclined 60° to horizontal appears in all R4 far-field maps. Its source is unknown, but with a relative magnitude of -60 dB it has negligible effect on convolved radiances. The horizontal strips result from aliasing due to insufficient sampling in the limb vertical (scanner horizontal) direction. For a few pairs of scans taken at different spacings, they move in accordance with the sampling theorem. These artifacts remained significant even with specialized MTI measurements, and had to be removed in preparing data for flight software as described below.

Patterns in all radiometers were compared before and after environmental tests. The most stringent comparison was for R4, whose RFE was also removed and re-installed between pattern sets. In this case patterns agreed to within 1 dB above -50 dB, and within 5 dB between -70 and -50 dB. The boresight co-alignment of R4 and R3 remained constant through tests within the measurement accuracy of $0.003°(3\sigma)$.

We characterized the scan angle dependence of FOV by measuring near-field patterns at 4 scan angles: ϵ =19.44°, 24.2°, 25.8° and 30.54° (tangent height h_T ≈300 km, 83 km, 0 km and -276 km, respectively). Test convolutions using these patterns gave scan angle dependences shown below (Table III) to be very small for normal atmospheric scan range (0–95 km) orbit, and degraded slightly for the total scan range.

Table II gives the beamwidth and beam efficiency ranges for all frequencies and scan angles measured before and after environmental tests. All values met performance requirements.

Since the limb radiance variation is significant only in the vertical direction over much less than the ±6° domain treated in Level 2 processing, measured FOVs were *collapsed* into the vertical plane (*i.e.* integrated over the horizontal direction)

TABLE II
MEASURED BEAMWIDTH AND BEAM EFFICIENCY RANGES OF THE GHZ FOVS, FOR ALL FREQUENCIES AND SCAN ANGLES MEASURED.

GHz Band	HPBW [min,max] / °		Beam Efficiency
	Vertical	Horizontal	[min,max]
118 R1A	[0.107,0.118]	[0.227,0.245]	[0.978,0.987]
R1B	[0.111,0.119]	[0.220,0.236]	[0.980,0.982]
190 R2	[0.074,0.084]	[0.147,0.168]	[0.959,0.980]
240 R3	[0.058,0.064]	[0.116,0.126]	[0.962,0.973]
640 R4	[0.0252,0.0271]	[0.0528,0.0572]	[0.962,0.967]

as in [8], to provide 1-dimensional FOV functions for the Level 2 forward model. Cross-polarized patterns which had to be substituted from nearby frequencies or scan angles were shifted in level, using the co-polarized peaks of their parent and the target patterns. Co- and cross-polarized patterns were collapsed separately for digital autocorrelator channels at the center frequencies of R1A and R1B, but combined in quadrature before collapsing, for all other bands. Figure 11 shows the result for the patterns of Figure 9, plus R1B patterns for comparison with R1A. The higher cross-polarized power of R1B is consistent with its RFE patterns and results from a less symmetric horn and higher feed mirror edge taper The bump at 3° appeared in several patterns of R1B, R2 and R3; we believe it is a range artifact, possibly reflection from a theodolite stand. Patterns with and without the bump were integrated with radiance kernels, showing a maximum error in convolved radiance of 0.01°; therefore we have not removed the bump from forward model FOV data. On the other hand, the large strips due to under-sampling, at 2.5° and 4.8° from the aperture center plane, had significant effect on convolved radiances and were removed from the collapsed patterns; interpolation across the gaps resulted in the four smooth patches in the R4 plot.

We convolved collapsed patterns with the radiance kernels and evaluated radiance errors for the range of scan angles and frequencies measured, to show compliance with the FOV calibration requirement.

The definitive determination of boresight direction (dFOV) was made by a theodolite survey of the alignment cube and the scanner immediately before or after a pattern measurement in the GHz pointing reference, whose band designation is B8LF:PT. This *fiducial* pattern was abbreviated to concentrate on main beam pointing rather than sidelobes. Interspersing fiducial patterns between those of other radiometers allowed the dFOV coincidence between radiometer FOVs to be evaluated quickly and without inflation of uncertainties which would result from going through an optical alignment data path. This method verified the co-alignment through environmental test, mentioned above.

During the definitive FOV calibration after environmental tests at JPL, dFOV was measured, along with the scan encoder reading, at the 4 scan angles listed above, to produce the the encoder/dFOV/cube calibration data. In later analysis, a time series of fiducial pointing information was constructed, to permit interpolation of reference pointing angles and scan

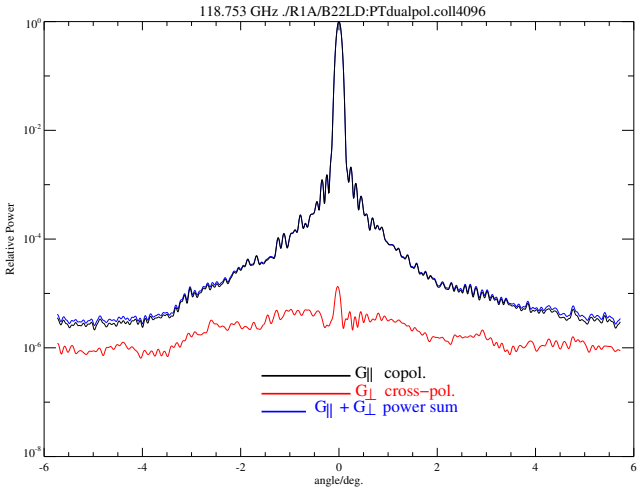

(a)

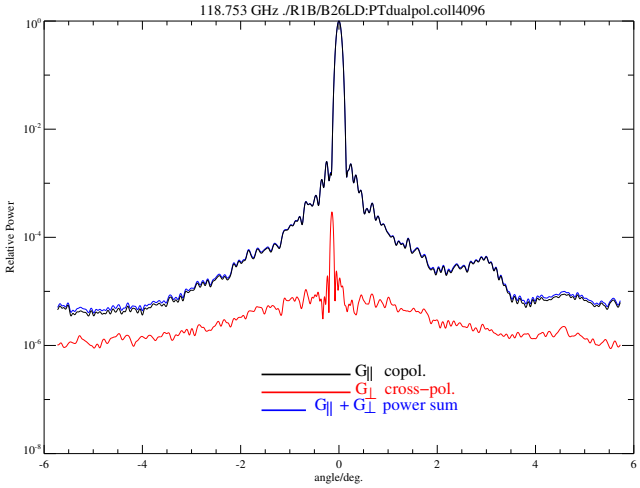

(b)

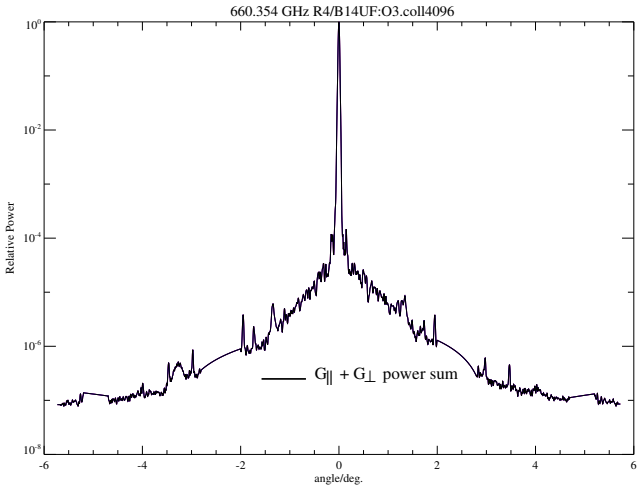

(c)

Fig. 11. Definitive FOV functions for Level 2 Processing Coefficients: (a) R1A and (b) R1B in both polarizations, and (c) R4 Band 14 unpolarized.

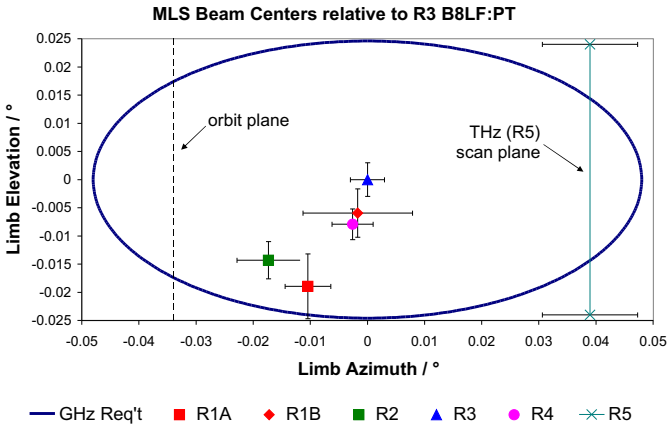

Fig. 12. Boresight coincidence of EOS MLS FOVs. Error bars include 3σ measurement uncertainty, variation with IF, and residual from the scan model fit of data taken at 4 scan angles. This view shows boresights projected onto a plane centered on the R3 limb tangent point, as seen from the MLS.

encoder readings onto the patterns of the other radiometers. A regression model was developed to fit heuristic misalignment parameters to dFOVs measured for each GHz radiometer, along with dFOV coincidence measured using fiducial patterns only. The results are combined with data, obtained during spacecraft integration, which give the boresight coincidence of GHz and THz pointing channels and their directions in spacecraft reference coordinates. Values for each band were provided to the flight software, and are plotted in Figure 12 as binned by radiometer. The grouping of boresight directions results from the tolerances on elements of the GHz optical multiplexer.

IV. In-Orbit Performance

All FOV-related engineering data observed during the activation of EOS MLS were within pre-launch predictions. Primary reflector temperatures matched predictions within 5° over the full $[-10, +75]^\circ$ C range (Aura's midsummer launch date made the angle β between sun and orbit plane near its minimum), as did the secondary and tertiary temperatures. With the scan stopped, a small relative rotation of the antenna, due to differing thermal expansion coefficients within the scan actuator and antenna under varying orbital heat loads, matched model predictions within 10–20 arcseconds.

For the following discussion of operation of the MLS, the repeat period of a scan through Earth's limb, nominally 24.7 seconds, is called a *major frame* (MAF). Most of the 240 MAFs per orbit each consist of 148 *minor frames* (MIFs), whose length is the instrument integration time, nominally 0.167 seconds. Scans of the GHz and THz modules start at the same time but cover different angles. As described in [3], a few MAFs just after Aura's descending node each have 1 MIF added to synchronize the remaining MAFs with the ascending node time, resulting in limb scans which occur at the same latitude each orbit.

A. Stray Radiances

Several tests performed in activation helped confirm the low stray light levels predicted before launch. These include:

periods of large amplitude scanning, a pitch-up maneuver (20° for 1/3 orbit and 5° for 3 orbits) to scan far sidelobes of the FOV over Earth's limb, and a slow sweep of the switching mirror through 360° with the antenna at a fixed scan angle. Among other things, this sweep checks for stray reflections within the switching mirror cavity and quantifies mirror angle sensitivity, for comparison with dual-cold load tests. Results of all these tests are still under study, but all show that stray-light FOV parameters in Table I have error bars at least as small as reported before launch, and we expect future calibration refinements to reduce these uncertainties.

1) Ohmic Loss corrections: Level 1 uses reflector temperatures, measured once per MAF at 17 points on the GHz reflectors, to calibrate radiances according to (3). Time series of high-altitude ($h_T > 87$ km) MIFs showed a ripple in the calibrated radiances having a shape similar to the average primary reflector temperature, suggesting that reflectivities in flight differed from the values measured before launch, by statistically significant amounts for R3 and R4. Compared to the pre-launch insertion loss results, flight ohmic losses appear slightly higher for R3 but lower for R4, which in the pre-launch data had been statistically the best determined. To explain this surprising finding we have assumed that, due to fabrication differences, the secondary and tertiary reflectors have greater reflectivities than the primary. Using high-altitude MIFs from days 210 and 245 of 2004, we retrieved new values for ohmic loss, relaxing the Fresnel constraint between the primary and the other reflectors, by making the average calibrated high-MIF radiance match the Planck value. Revised values for all radiometers, shown in Table I, were included for version 1.5 of the MLS flight software (the version producing the first publicly released data).

We are continuing to review these values, in particular to resolve the remaining orbital ripple into ohmic and spillover components. We are also devising laboratory measurements, using the engineering model R4 receiver, to understand the dependence of ohmic loss on incidence angle, polarization and reflector construction.

2) Stability of Space View Radiance: Since the GHz space view points opposite to Aura's orbit normal vector, the Moon contaminates the space view for $\sim$ 20 hours about twice a year, by up to 4 K radiance for the worst geometry. Figure 13 is a time series of radiances in selected bands of R1A, R2 and R3 averaged over high-altitude MIFs on day 355 of 2004, showing the stability of the space view at the onset of the Moon's entry into the center of the space beam. Higher noise masks a similar shape for R4. The same plot for the next day is roughly reversed, as the Moon spirals out of the beam. Curves in the left half of this plot show the residual ripple after the correction of ohmic losses; determining the source of this residual is the subject of our current calibration refinement, although dynamic baseline corrections in Level 1 allow later processing steps to remove most of this spectrally invariant offset. Using simplified forms of a Moon radiance model described below, we can predict the radiance contamination within about 0.2 K, so we are also customizing local versions of the Level 1 software in attempts to reclaim the data lost during these events.

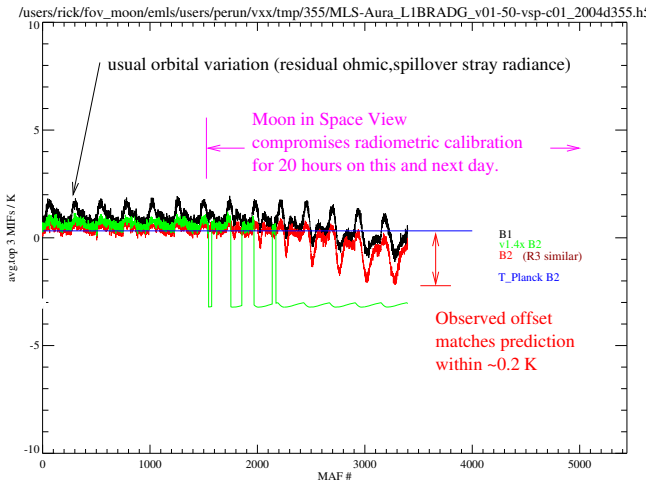

Fig. 13. Time series of high-altitude MIFs on day 355 of 2004, showing residual orbital variation after corrections to ohmic losses, and at right the Moon entering the GHz space view after MAF 1500.

B. Moon Calibration of pointing offsets

Retrieved profiles of atmospheric constituents depend on knowledge of radiometer FOV offsets (dFOV) relative to the pointing reference (B8LF:PT for EOS MLS) [17]. During early months of the UARS mission, discrepancies between retrieved ozone profiles from two UARS MLS radiometers were attributed to errors in pre-launch values of relative pointing. This led us to use the Moon as a pointing calibration source to establish offsets between in-flight radiometer FOVs [8]. For EOS MLS, the 0.003° measurement uncertainty we found for pre-launch dFOV corresponds to a 1% error in profile magnitude, somewhat less than the differences found in current MLS retrievals and intercomparisons [17]. To confirm our pre-launch values of dFOV coincidence and to reduce their uncertainties, we have begun a series of Moon scans for EOS MLS, similar to those done for UARS MLS.

The Moon crosses Aura's orbit plane twice per month, with lunar phases within a few degrees of -155° ($\sim$new Moon) and +25° ($\sim$full Moon). Given the periods of the Moon and Aura, the scan ranges of THz and GHz FOVs cross the lunar disk on about 60% of these opportunities. As of this writing, we have replaced the nominal atmospheric scan with a special scan, well above the atmosphere, for six of these events. The scan moves the THz and GHz FOVs in opposing "sawtooth" scans; their ranges are chosen to guarantee that each will have at least one string of 30 or more Limb MIFs viewing the Moon, and two if the Moon does not appear in calibration views.

Algorithms for retrieving pointing offsets from Moon radiances were developed for UARS MLS [8]. Measured radiances are compared to radiances, predicted from an Apollo-based lunar microwave model [18], that are convolved with the 2-dimensional measured FOVs, swept over the face of the Moon during the $\sim$0.167 s integration time. We can relate measured radiances to the model map and its gradient by two pointing angles and a scaling factor A_M. These 3 parameters are estimated by minimizing the sum of squared radiance residuals for the $\sim$60 MIFs in each Moon crossing. Unlike UARS MLS,

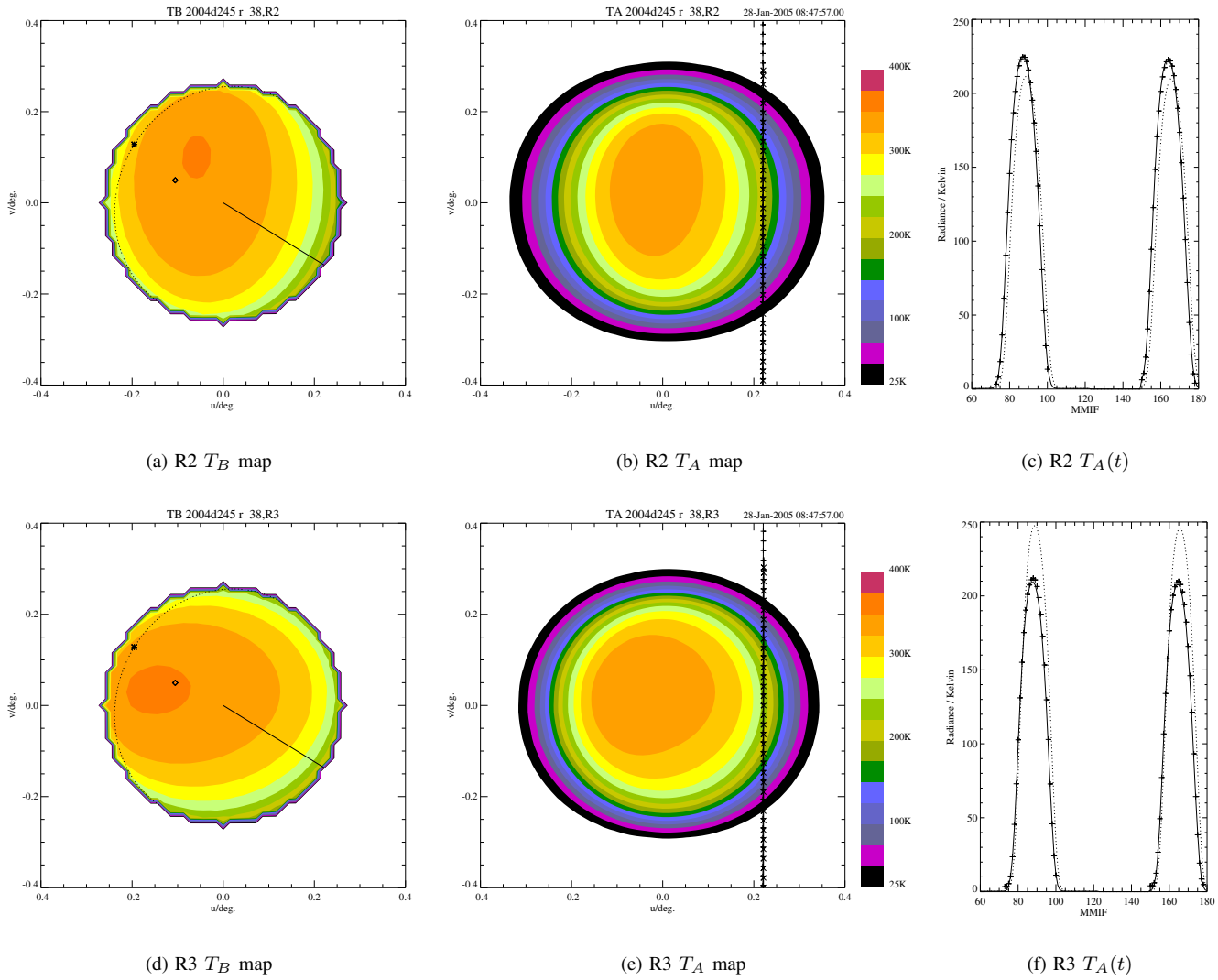

(a) R2 T_B map (b) R2 T_A map (c) R2 $T_A(t)$

(d) R3 T_B map (e) R3 T_A map (f) R3 $T_A(t)$

Fig. 14. Example of FOV scan through Moon on day 245 of 2004, for 190 GHz (a–c) and 240 GHz (d–f). We are extending the Moon radiance model to the other MLS frequencies. (a,d) are model radiances T_B incident on the MLS antenna, showing polarization dependence and model angular resolution; (b,e) show convolved limb radiance T_A with scan pattern; (c,f) are radiance time series $T_A(t)$ versus MIF before (dashed) and after (solid) iterative solution for dFOV. In this example the model scale factor A_M was retrieved (not constrained as usual) to show its coupling to the azimuth pointing u.

the EOS MLS FOVs move across the Moon only in the limb vertical direction, so the retrieval has difficulty distinguishing A_M from limb horizontal misalignment;[3] hence we generally constrain $A_M \equiv 1$.

A typical result is in Figure 14, showing Moon model radiance maps before and after convolution with the MLS FOVs in R2 and R3. These data are still being analyzed, but preliminary results indicate the THz FOV is pointing $0.007 \pm 0.003^\circ$ (350 ± 150 m) higher in the atmosphere than the GHz FOV, after encoder angles are corrected for all misalignments known before launch. The same uncertainty applies to dFOV coincidences between radiometers within the GHz module, which validates the pre-launch values of Figure 12 to the accuracy of the near field measurements. We are currently extending the UARS MLS model from 63–205 GHz to 2.5 THz, which we expect to yield error bars of the same order for EOS MLS ($3\sigma = 0.0006^\circ$).

[3]The matrix condition number, a measure of retrieval singularity, is typically $10\times$ greater than for the UARS MLS Moon scans.

V. Conclusions

This paper has described the GHz optics design and calibration. Ground calibration provided all FOV parameters and functions required for flight data processing. In-flight evaluation of these is still in progress, but so far has validated all these except ohmic loss, some of whose values we have revised using in-flight data and provided for the current version of flight software. We are developing a laboratory measurement program to corroborate these changes.

Table III summarizes systematic uncertainties in FOV. Scaling uncertainties have been separated from radiance offsets, which are removed by Level 2 processing. The principal contributions to scaling uncertainty are ohmic loss uncertainty and the variation (with IF) of the difference between limb and space beam solid angles from the feed patterns. The table also contains estimates of uncertainties in the detailed FOV

TABLE III
SUMMARY OF FOV UNCERTAINTIES

	R1A	R1B	R2	R3	R4
Level 1 scaling uncertainty (3σ)	0.17%	0.23%	0.20%	0.21%	0.38%
HPBW uncertainty (3σ)	0.004°	0.006°	0.002°	0.001°	0.0015°
Pointing offset uncertainty (all GHz and THz relative to B8LF:PT)					
Pre-launch + crude Moon model	$\pm 0.003°$				
expected from refined Moon model	$3\sigma = 0.0006°$				
Error in convolved radiance due to scan dependence of FOV / K					
$h_T \in [0, 83]$ km	± 0.15	± 0.12	± 0.09	± 0.16	± 0.24
$\in [-280, 300]$ km	± 0.4	± 0.3	± 0.4	± 1.2	± 0.27

patterns. Since the small frequency dependences within each radiometer have been captured by providing band-dependent patterns to the flight software, the remaining uncertainty is dominated by residual scan angle dependences, themselves also small as shown.

The GHz optics and FOV calibration have met all requirements, and we continue to maintain and refine calibrations through the duration of the mission.

ACKNOWLEDGMENT

The authors wish to acknowledge the work of many members of the MLS science and instrument teams whose contributions made the design and FOV calibration of the GHz optics possible. We would especially like to thank Janet Squires for developing the NASTRAN deformations model; Nasrat Raouf for help with the optics model and feed mirror procurement; Eugene Poyorena, Mark Thompson, and Nick DeLuca for theodolite and opto-mechanical measurements in all assembly phases; Jack Hardy, Robert Dengler and Ray Swindlehurst for support of receiver patterns, and for help in the conception and implementation of the near field range, as well as Dan Slater and Greg Hindman of NSI; and other colleagues too numerous to mention here. We also particularly thank Stephen Keihm for enhancing the Moon radiance models from UARS frequencies up to 2.5 THz.

REFERENCES

[1] J. W. Waters *et al.*, "The EOS Microwave Limb Sounder (MLS)," *IEEE Transactions on Geoscience and Remote Sensing*, vol. This issue.
[2] ——, "The Upper Atmosphere Research Satellite and Earth Observing System Microwave Limb Sounder Experiments," *Journal of the Atmospheric Sciences*, vol. 56, pp. 194–218, January 1999.
[3] H. M. Pickett, "Microwave Limb Sounder THz Module on Aura," *IEEE Transactions on Geoscience and Remote Sensing*, vol. This issue.
[4] W. G. Read, Z. Shippony, M. J. Schwartz, and W. V. Snyder, "The Clear-Sky Unpolarized Forward Model for the EOS Aura Microwave Limb Sounder," *IEEE Transactions on Geoscience and Remote Sensing*, vol. This issue.
[5] R. F. Jarnot and M. J. Schwartz, "Radiometric and Spectral Performance and Calibration of the GHz Bands of Aura MLS," *IEEE Transactions on Geoscience and Remote Sensing*, vol. This issue.
[6] F. T. Barath *et al.*, "The Upper Atmosphere Research Satellite Microwave Limb Sounder Instrument," *Journal of Geophysical Research*, vol. 98, no. D6, pp. 10,751–10,762, June 1993.
[7] J. Ruze, "Antenna tolerance theory—a review," *Proceedings of the IEEE*, vol. 54, no. 4, pp. 633–640, April 1966.
[8] R. F. Jarnot *et al.*, "Calibration of the Microwave Limb Sounder on the Upper Atmosphere Research Satellite," *Journal of Geophysical Research*, vol. 101, no. 6, pp. 9957–9982, April 1996.
[9] P. Siegel, R. Dengler, and J. Chen, "THz dichroic plates for use at high angles of incidence," *IEEE Microwave and Guided Wave Letters*, vol. 1, no. 1, January 1991.
[10] F. T. Ulaby, R. K. Moore, and A. K. Fung, *Microwave Remote Sensing, Active and Passive*. Addison-Wesley, 1981.
[11] D. Slater, *Near Field Antenna Measurements*. Artech House, Inc., 1991, ISBN 0-89006-361-3.
[12] D. Slater *et al.*, "A large aperture 650 GHz near-field measurement system for the Earth Observing System Microwave Limb Sounder," in *Antenna Measurement Techniques Association Conference20th ESTEC Antenna Workshop on Millimetre Wave Antenna*, Oct. 2001.
[13] P. Stek and R. Cofield, "Near-field measurements of a high gain 110 to 660 ghz antenna for remote earth sensing," in preparation.
[14] G. Hindman *et al.* (2004) Nearfield systems homepage. Nearfield Systems, Inc. [Online]. Available: http://www.nearfield.com
[15] N. Erickson and V. Tolls, "Near-Field Measurements of the SWAS Antenna," in *20th ESTEC Antenna Workshop on Millimetre Wave Antenna Technology and Antenna Measurements*, Noordwijk, The Netherlands, June 18–20, 1997.
[16] D. Slater. (1995, May) Three-axis motion tracking interferometer for measurement and correction of positional errors between an article under test and a measurement probe. United States Patent 5419631. [Online]. Available: http://www.nearfield.com/Patents/tmt.htm
[17] L. E. Froidevaux *et al.*, "Early Validation Analyses of Atmospheric Profiles of EOS MLS on the Aura Satellite," *IEEE Transactions on Geoscience and Remote Sensing*, vol. This issue.
[18] S. Keihm, "Interpretation of the lunar microwave brightness temperature spectrum: Feasibility of orbital heat flow mapping," *Icarus*, vol. 60, pp. 568–589, 1984.

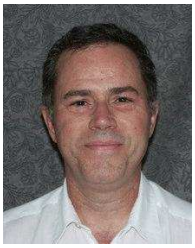

Richard E. Cofield (M'83) received the B.S. degree in Applied Physics from the California Institute of Technology in 1974, and the M.S. degree in Electrical Engineering from the University of Southern California in 1982. In 1978 he joined the Jet Propulsion Laboratory, Pasadena, California, to design, analyze and calibrate antenna and optical systems for spaceborne radar and radiometer instruments observing the Earth. His interests include reflector antennas and quasi-optical feed systems.

Paul C. Stek (Ph.D.'97) received the B.S. degree in Engineering Physics from the University of California at Berkeley in 1986, and the Ph.D. degree in Physics from the Massachusetts Institute of Technology in 1997. In 1997 he joined the Jet Propulsion Laboratory, Pasadena, California, to develop millimeter and sub-millimeter wave technology for remote sensing. His interests include radiometer development and calibration.